Chapter 43
Fractal Electronics for Stimulating and Sensing Neural Networks: Enhanced Electrical, Optical, and Cell Interaction Properties

S. Moslehi, C. Rowland, J. H. Smith, W. J. Watterson, W. Griffiths, R. D. Montgomery, S. Philliber, C. A. Marlow, M.-T. Perez, and R. P. Taylor

Abstract Imagine a world in which damaged parts of the body – an arm, an eye, and ultimately a region of the brain – can be replaced by artificial implants capable of restoring or even enhancing human performance. The associated improvements in the quality of human life would revolutionize the medical world and produce sweeping changes across society. In this chapter, we discuss several approaches to the fabrication of fractal electronics designed to interface with neural networks. We consider two fundamental functions – stimulating electrical signals in the neural networks and sensing the location of the signals as they pass through the network. Using experiments and simulations, we discuss the favorable electrical performances that arise from adopting fractal rather than traditional Euclidean architectures. We also demonstrate how the fractal architecture induces favorable physical interactions with the cells they interact with, including the ability to direct the growth of neurons and glia to specific regions of the neural–electronic interface.

Keywords Fractals · Human implants · Electronics · Neurons

S. Moslehi · C. Rowland · J. H. Smith · W. J. Watterson · W. Griffiths · R. D. Montgomery ·
S. Philliber · R. P. Taylor (✉)
Physics Department, University of Oregon, Eugene, OR, USA
e-mail: rpt@uoregon.edu

C. A. Marlow
Physics Department, California Polytechnic State University, San Luis Obispo, CA, USA

M.-T. Perez
Department of Clinical Sciences Lund, Division of Ophthalmology, Lund University, Lund, Sweden

43.1   Introduction

In 1752, Benjamin Franklin attached a metal key to the bottom of a dampened kite string and then flew the kite in a storm. It didn't take long to go from his simple demonstration of harnessing electricity to applying it to living bodies. In 1764, physician Charles Le Roy applied electricity to patients' eyes, causing them to see flashes of light. In 1791, Luigi Galvani did the same to the muscles of frog legs, causing them to twitch [1]. Since then, two centuries of rapid development have led to today's commercial electronics industry. Miniaturization has been the main driver of improvements. In addition to faster operation, the evolution from micro-electronics to nano-electronics facilitates novel methods for manipulating the flow of electricity. For example, our research group has investigated ballistic electronics [2], quantum electronics [3], spin electronics [4], and coulomb blockade [5]. However, developments such as these target the computing and communications industry rather than electronic interfaces with biological systems.

Miniaturization offers surgeons the opportunity to implant devices in humans rather than relying on the crude external wires used by Le Roy and Galvani. For example, electronic devices have been implanted into human retinas with the aim of restoring vision to patients with degenerative retinal diseases [6–13]. More than 150,000 deep brain stimulation implant surgeries have been performed targeting neurological disorders such as Parkinson's disease [14]. Furthermore, people with amputated limbs receive interactive prosthetic implants that restore mobility. In addition to enhancing the performance of medical devices, exploring neuron responses to implants can be used to investigate their fundamental behavior and the degree to which this behavior can be controlled. Such studies should also accommodate interactions with glia. Although neurons and glia were discovered around the same time, research on the latter has been slower to gain momentum [15] even though they are prevalent in the central nervous system [16] and play central roles in controlling neuronal network structure and functionality [17]. Specifically, whereas neurons are crucial for carrying the body's electrical signals, glia are equally crucial because of their supporting role as the neurons' life support system.

Significantly, implants are frequently referred to as bionic devices in recognition of the importance of bio-inspiration and the need for biocompatibility at the cell–implant interface ("bion" is Greek for "unit of life"). Yet, Fig. 43.1 highlights a fundamental geometric mismatch between today's conventional implants and the cells that they interact with. Confocal microscopy (Fig. 43.1a) can be used to construct three-dimensional models of neurons (Fig. 43.1b), allowing an analysis of their fundamental geometry [18–20]. Discussed in more detail in Chap. 44, this analysis shows that neurons belong to fractal geometry, featuring dendritic branches that repeat at increasingly fine-size scales. In contrast, the active area of typical implants is based on Euclidean geometry. The gray square shape shown in Fig. 43.1c serves as an example.

Fractal branches are prevalent in nature. When flying his kite in the storm, Franklin would have noticed the multi-scaled branches of the lightning around him,
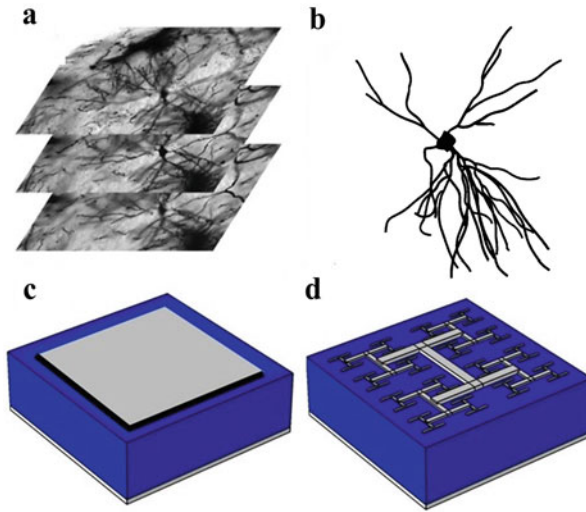
Fig. 43.1 (**a**) Confocal microscopy generates a stack of 200 μm × 200 μm horizontal sections (with vertical separations of 2 μm) of Golgi-Cox-stained neurons. (**b**) These sections are then computer-assembled into three-dimensional images for pattern analysis. A neuron's basal dendrites from a rat's hippocampus are shown for demonstration. (**c**) A schematic showing the square-shaped active area (light gray) of a conventional implant. (**d**) For our bio-inspired implants, the active area features branched patterns that repeat at different size scales

along with the fractal trees that populate many natural environments. Animals also benefit from fractal branches in, for example, their bronchial trees and veins. In each case, as their branches spread out in space, the structure features two embedded fractal patterns – the branches and the gaps forming between them. Their structural relationship offers the potential to balance functionality with operational costs while also maintaining structural integrity. In this balancing process, the repeating patterns offer large interfaces to interact with light in the case of trees [21], oxygen in the case of bronchial trees [22], and neighboring cells in the case of neurons [18].

Even if Franklin had pondered the potential benefits of using a set of strings that copy lightning branches, the challenges of assembling this network would have been daunting enough to dampen his enthusiasm for such an experiment. In contrast, here we will present state-of-the-art approaches to fabricating fractal electronics suitable for implants. Adopting the principle of bio-inspiration, we will describe the use of fractal interconnects to establish a biophilic interface between the implants and the neuronal cells they interact with. A repeating H-pattern is shown as an example in Fig. 43.1d. We will consider fractal interconnects with two distinct electrical functions – electrodes that stimulate signals in the neurons and sensors that detect and track these signals as they pass through the body's neural network. The superior electrical, optical, and physical properties of the fractal interconnects are expected to be generic. Future applications could therefore include interactions with neuronal cells in the brain, retina, and limbs.

43.2   Fabrication of the Fractal Interconnects

When neuronal cells interact with each other, they do so by exploiting both their physical and chemical environments. Our interconnects aim to do the same. We exploit carbon nanotubes (CNTs) as our interconnect material. A wealth of previous research has studied interactions of CNTs with many cell types, including neurons. Their density, stiffness, and topography can be controlled [23–25], and they can be synthesized on, or transferred to, flexible substrates [26, 27]. Due to a combination of their chemical composition and surface texture, CNTs promote neuronal adhesion and increase the number of processes and their growth [28–30]. Their nanoscale roughness has been proposed to mimic some of the extracellular matrix (ECM) properties [31, 32] and to enhance neurite outgrowth and elongation if the roughness variation matches the neuron process diameter [33]. CNT flexibility also likely plays a role, since neurons are known to readily adhere to and grow processes on softer substrates [34, 35].

Although it has been suggested that CNT functionalization is necessary for biocompatibility, our research supports previous results demonstrating that appropriate degrees of texture and flexibility of our pristine CNTs are sufficient for neural network survival [36], which in turn favors recording and stimulation [37]. Previous studies demonstrating that electrically biased CNT electrodes stimulate neurons effectively [38, 39] and even boost their signal transmission [40, 41] indicate that our fundamental studies have large potential for translation to future applications.

We employ two fabrication techniques to match the fractal geometry of the CNT interconnects and the neurons. Whereas all fractals exhibit repetition of patterns at multiple size scales, fractals can be grouped into two categories based on how the patterns repeat. For fractals prevalent in the body (e.g. neurons, veins, and bronchial trees), the statistical qualities of the patterns repeat at different scales. In contrast, the patterns of mathematically generated "exact" fractals repeat exactly at different scales. Consequently, whereas exact fractals look precisely the same at increasingly fine scales, "statistical" fractals simply look similar at different scales [42]. One of our fabrication techniques exploits the precision and control associated with the clean geometry of exact fractals. The other harnesses natural deposition processes to generate statistical fractals.

Fractal dimension, D, is a central parameter for quantifying both types of fractal. This describes how the patterns occurring at different scales combine to build the resulting fractal shape [42]. For Euclidean shapes, dimension is described by familiar integer values – $D = 1$ for a smooth line and $D = 2$ for a completely filled area. The repeating patterns of a fractal line cause the line to begin to occupy more space than the Euclidean line. This occurs at multiple scales and results in a D value that has a non-integer value lying between 1 and 2. For each fabrication method, D can in principle be adjusted along with the size scales over which the fractal repetition occurs. This facilitates an investigation of the impact of these fractal parameters on the interconnects' properties.

Fig. 43.2 Scanning electron micrograph (SEM) images of patterned VACNT forests. (**a**) Top-down view of entangled VACNTs on the forest's top surface. (**b**) and (**c**) are views of VACNT sidewalls taken at a 40° angle. Scale bars are 2, 10, and 20 μm, respectively. The VACNT patterns are fabricated in collaboration with B. Alemán (University of Oregon, USA)
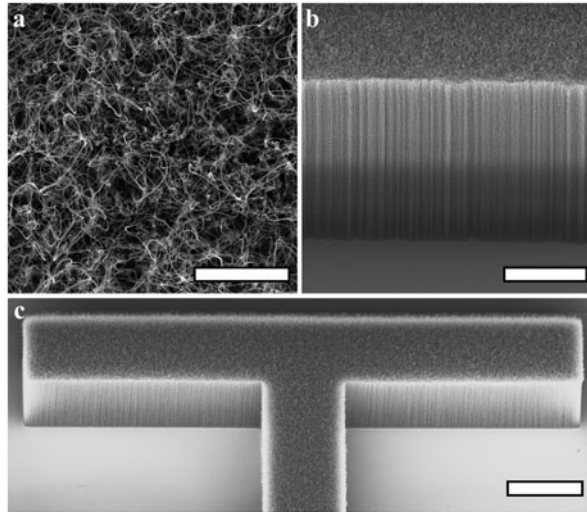
To construct the exact fractals, we employ a vertically aligned CNT (VACNT) approach in which CNTs grow vertically to heights of approximately 25 μm from a metallic catalyst layer deposited on a smooth silicon dioxide (SiO_2) substrate [43]. Crucially, they tangle into a conducting "forest" as they grow (Fig. 43.2). These forests can be shaped laterally by using lithography to define intricate patterns in the catalyst layer. In addition to establishing textured branches separated by smooth gaps, the high aspect ratios of the VACNTs will aid penetration into neural tissue [44]. The gap sizes span from a few μm up to ~4 mm to investigate both the individual and cell network interactions with the interconnects (retinal neuronal and glial cell bodies range from a few μm to ~30 μm, and glial and dendritic processes can be as large as a few hundred micrometers). The VACNT branch width is chosen to be $W_{CNT} = 20$ μm to allow the somas of several neurons to attach to the VACNT surfaces and for their processes to grow out from the somas across the electrode surface.

We choose the H-Tree (built from repeating H-patterns) for the lateral shape because it is an established branched fractal with well-defined scaling properties. As demonstrated in Fig. 43.3, D sets the rate of shrinkage of branch length between repeating levels with a higher D corresponding to a slower rate. In addition to D, the number of repeating levels m is varied (Fig. 43.3). Acknowledging that even these simple H-Trees are inherently complex, we also investigate interconnects consisting of rows and grids. We refer to these comparators as Euclidean designs because the gaps within each interconnect design have a single scale in contrast to the multi-scale character of the fractal design. For the rows, W_{CNT} and the gap width, W_{Si}, vary between interconnects and span from 25 to 100 μm. For the grids, $W_{CNT} = 25$ μm to match the fractal design and $W_{Si} = 60$ μm is chosen to ensure that each grid's "cell" can accommodate several glial cell bodies.

Fig. 43.3 The left column
from top to bottom shows
schematics of the fractal, row,
and grid interconnects:
($D = 1.1$ and $m = 4$, labeled
as 1.1–4), ($D = 1.5$ and
$m = 4$, labeled as 1.5–4),
($D = 2$ and $m = 4$, labeled as
2–4), ($D = 2$ and $m = 5$,
labeled as 2–5), ($D = 2$ and
$m = 6$, labeled as 2–6),
(Row), and (Grid). The right
column shows SEM images
of a region of the interconnect
shown in the left column. The
fractals and the first image of
rows are shown from a top
view, while the second row
and grid images are taken at a
40° angle. From top to
bottom, the scale bars are
100, 200, 400, 200, 200, 100,
200, and 50 μm. The VACNT
patterns are fabricated in
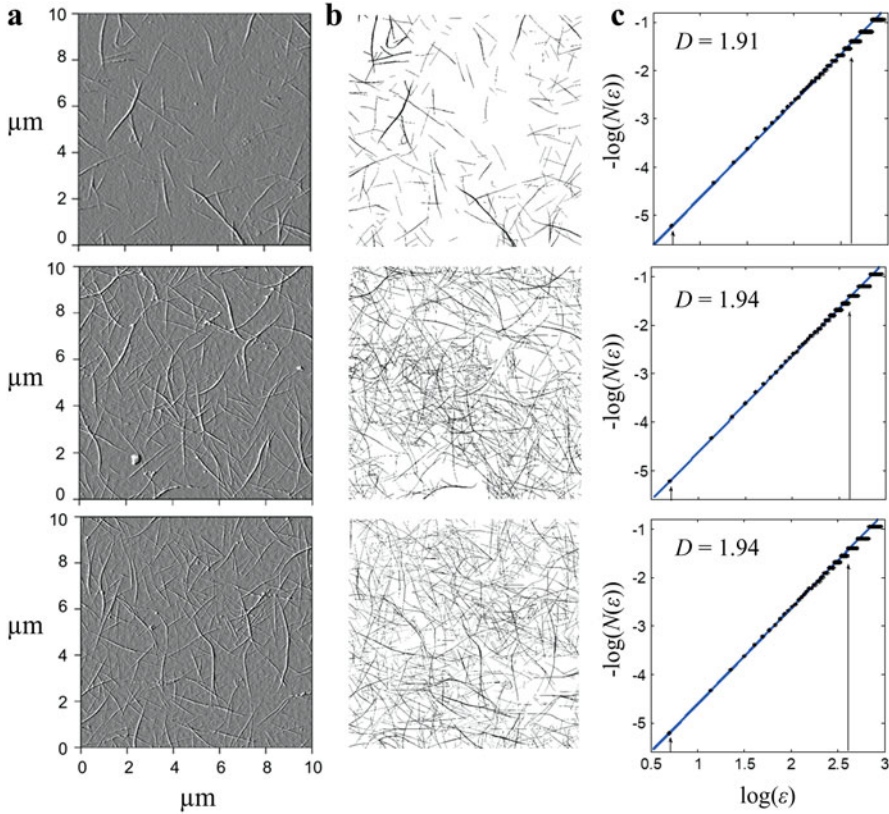collaboration with B. Alemán
(University of Oregon, USA)
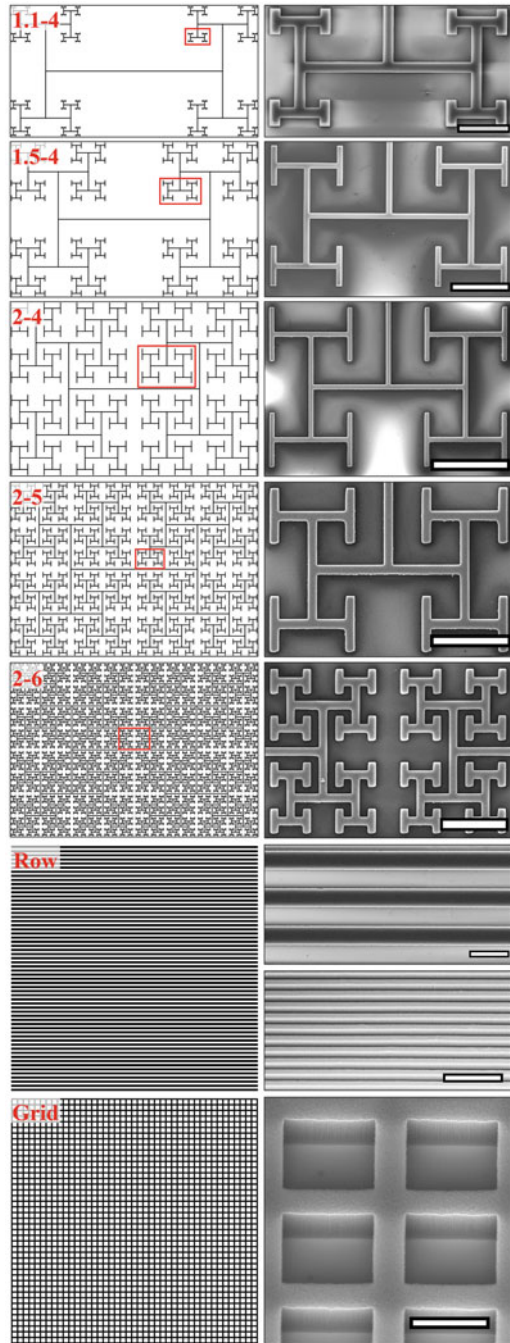
Fig. 43.4 Fractal analysis of the CNT thin film network. (**a**) AFM images of typical networks. (**b**) To perform the fractal analysis, these images are converted to black and white bitmap images. (**c**) The associated box-counting fractal analysis plots in which the log of the minimum number of boxes, $N(\varepsilon)$, required to cover the network is plotted against box size, ε. The arrows indicate the expected limits to assess D. The CNT films are fabricated in collaboration with N. Plank (University of Victoria, New Zealand)

To fabricate the statistical fractals, a thin horizontal film (spanning 3 mm × 7 mm with thickness varying between 1.5 and 10 nm depending on bundling) of CNTs is formed on a SiO_2 substrate using a solution deposition technique [45–48]. To confirm that these randomly arranged CNTs self-assemble into a statistical fractal network, a standard box-counting technique is performed on atomic force microscope (AFM) images of the networks. Figure 43.4 shows three examples of 10 μm × 10 μm images taken at different locations on the film. In each case, the image is covered with a mesh of identical squares (boxes). For a network to be considered fractal, the minimum number of boxes, $N(\varepsilon)$, required to cover the network scales according to box size, ε, as $N(\varepsilon) \sim \varepsilon^{-D}$. The linearity of the plot indicates the networks are fractal. A higher D fractal corresponds to a steeper

Fig. 43.5 Probability of percolation, %, (**a**) and fractal dimension, D, (**b**) of 100 and 5 simulated CNT thin film networks for (**a**) and (**b**), respectively, as a function of stick density ρ. The top images show networks connected to measurement terminals located along the network's perimeter (symbolized by eight yellow squares). The nonlinear character of the networks is highlighted by coloring according to the number of sticks needed to connect the upper left and lower right terminals to the given stick: red indicates sticks that are not connected to the network, yellow indicates a small number of sticks, and dark blue indicates a large number
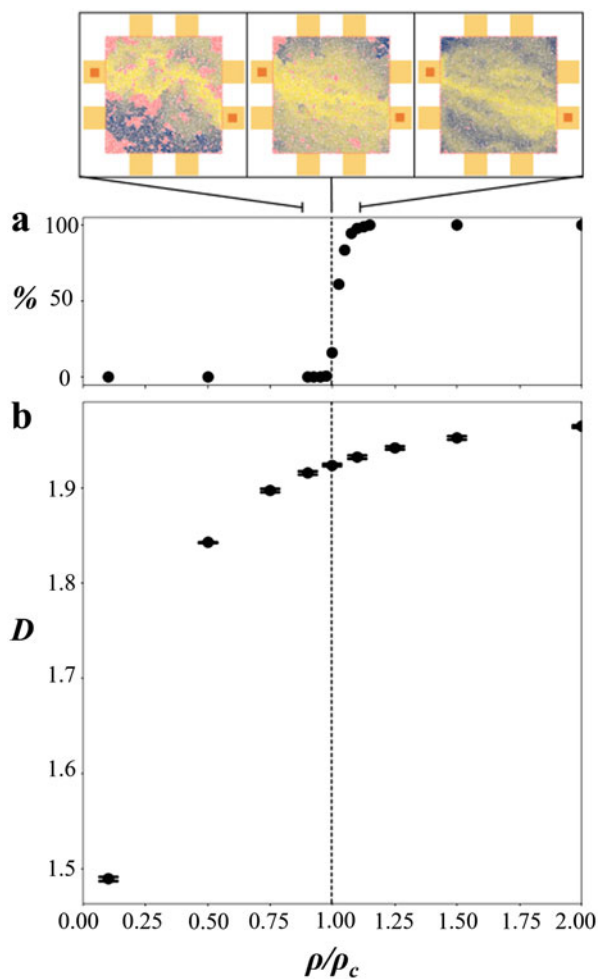
slope and therefore to the pattern occupying a larger number of fine-scale boxes. The observation limits are shown by the arrows. As expected, the lower limit of observation is set by the smallest feature size and the upper limit set by the counting statistics of the box-counting algorithm (20% of the total network size).

The average tube lengths for the shown films are (from top to bottom) 1.6, 1.9, and 1.9 (± 0.5) μm with associated tube densities of 3.0 tubes (± 0.5)/μm^2, 9.9 tubes (± 0.9)/μm^2 and 9.9 tubes (± 0.9)/μm^2, respectively. To demonstrate the relationship between density, r, and D more systematically, Fig. 43.5 shows the results of a Monte Carlo simulation of the deposition process [49] in which "sticks" (representing either individual or small bundles of CNTs) have a fixed length approximating to the tubes within our CNT network. The vertical dashed line indicates that the stick density ρ_c is necessary for an infinite system to reach

its percolation threshold (i.e. to establish an electrical connection by at least one continuous path across the network). However, Fig. 43.5a plots the probability, %, that our finite-sized network will establish percolation and demonstrates that a higher density than the dashed line value is necessary to reliably establish electrical connectivity across the network.

Figure 43.5b shows the average D for simulations and reveals a clear dependence on ρ. Near the percolation threshold, D changes rapidly and then saturates at higher densities. When interpreting the shape of this curve, recall that D is an indicator of the ratio of fine to course structure in the network. As more tubes are added to the network its fine structure increases, raising the D value. Taken together, Figs. 43.4 and 43.5 demonstrate the potential of tuning the fabricated network's D value using deposition density. Furthermore, the film could be patterned post-synthesis by etching away selected regions. Alternatively, the tip of an AFM could be scanned across the nanotube network while applying an electrical bias to the tip, which would cut the network into the desired fractal pattern.

43.3 Functionality of the Fractal Interconnects

Our interconnects are designed to serve two distinct electronic functions – inducing and detecting electrical signals in the neurons. For both functionalities, it is crucial to consider the impact of the fractal design on the mechanical, optical, and electrical properties of the neuron–implant interface along with its impact on cell health and growth. Adopting the philosophy that the implant is only as strong as its weakest link, we target the fundamental science that emerges when all of these properties are considered in unison. In terms of their mechanical properties, fractal circuits have been proposed for stretchable electronics [50] – the associated flexibility therefore presents the possibility of developing future interconnects that are conformal to the regions of the neural network in which they are implanted. In terms of optics, the surface coverage of the fractal interconnects is considerably less than the equivalent squares due to the multitude of gaps between the branches (Fig. 43.1c and d). This suggests that light can be easily transmitted through the fractal interconnect. This will be advantageous for future brain implants that utilize both optical and electrical stimulation [51]. Furthermore, the ability to shine light through the interconnects is crucial for the operation of retinal implants featuring interconnects positioned above photodiodes [52].

The interconnects' electrical properties are central to the operation of both stimulators and sensors. Electronic stimulation of neurons dates back to the pioneering studies of Le Roy and Galvani. The electrical fields from their electrodes set up potential differences across the neuron membrane, inducing ion flows that trigger a signal along the axon [53]. In Le Roy's experiment, for example, this process induced signals in the retinal neurons that the brain interpreted as originating from the retina's photoreceptors. The positive impact of adopting the fractal geometry becomes clear by returning to the schematic of Fig. 43.1c and d in which the gray
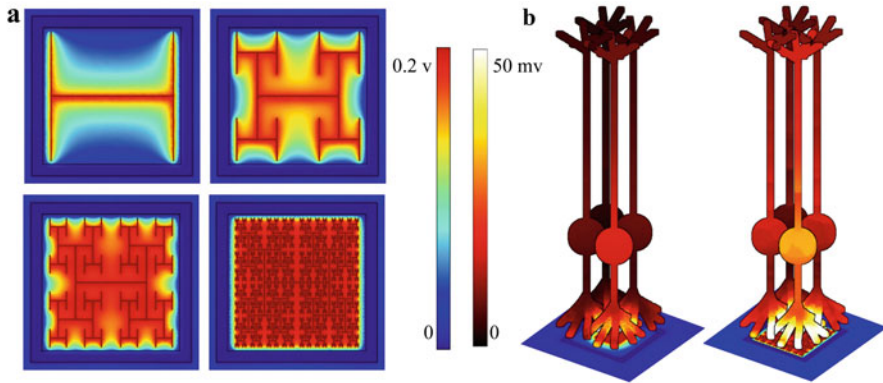
Fig. 43.6 Simulations of electric fields generated by a shaped central electrode surrounded by a ground electrode (the latter is not shown for clarity). (**a**) Color plots showing a horizontal slice (at the central electrode's top surface) of the three-dimensional voltage distribution for an H-Tree central electrode. The four simulations show the field uniformity achieved by increasing the repetition levels from $m = 1$ to $m = 4$. In each case, the applied voltage is 0.2 V and the frequency is 1 kHz. The left central color bar shows the maximum extracellular voltages reached during each oscillation which varies from 0 V (blue) to 0.2 V (red). (**b**) A color plot of the maximum change in electric potential across the membrane before and after stimulation for bipolar neurons above a square central electrode (left) and fractal central electrode (right) both for an applied bias of 0.2 V and a frequency of 1 kHz. The right central color bar displays the magnitude of the potential and varies from 0 V (black) to 50 mV (white). For visual clarity, only four of the nine neighboring neurons are shown. Images are drawn to scale: the neurons are 100 μm in height, and the soma is centered 30 μm above the surface

interconnect serves as the stimulating electrode. Our simulations of the electrostatic properties of electrodes show that a significant amount of electrical charge resides on the sidewalls of the electrodes [54]. The simulations in Fig. 43.6 demonstrate that the increase in sidewall charge with m results in increasingly uniform fields such that a $m = 4$ fractal electrode's electric field is as uniform as that of an electrode without gaps. Consequently, the gaps can let light through without disrupting the field. Compared to traditional Euclidean electrode designs such as grids and squares, the large boundaries inherent in fractal patterns generate a large surface area at the sidewalls. The enhanced electrical capacitance then results in larger stimulating electric fields. For the 20 μm × 20 μm electrodes designed for retinal implants, our simulations demonstrate that voltage biases that stimulate all of the neighboring neurons when applied to the fractal electrode stimulate less than 10% of them when applied to the equivalent square electrodes (Fig. 43.6) [55]. This fractal advantage translates to electrodes applicable to brain stimulation applications.

The growth conditions that we use for the VACNTs generate multi-walled CNTs that are metallic [56] and therefore ideal for electrode applications (due to their low resistances, metals minimize variations in electrostatic potential across the electrode). In Fig. 43.7, we show how the large-scale H-Tree design (which purposely spreads across millimeter scales to interact with large neural networks) of
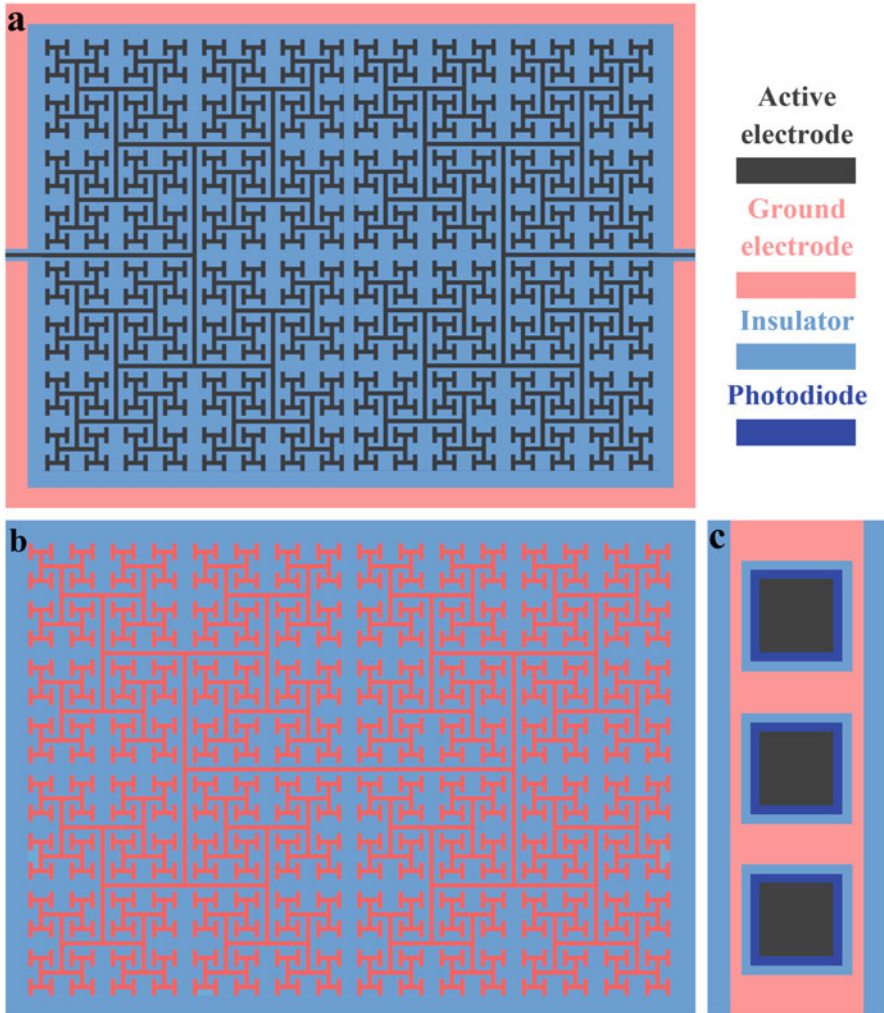
Fig. 43.7 Potential electrode designs for brain and retinal stimulation purposes. (**a**) For brain stimulation purposes, the large-scale fractal pattern (gray) serves as the active electrode bounded by a rectangular ground electrode (pink). (**b**) For retinal stimulation purposes, the large-scale fractal pattern serves as the ground electrode (pink) with an array of small holes inserted along its branches. (**c**) The zoom-in on a fractal branch in (**b**) shows three holes within the branch of the ground fractal electrode. Each hole features an active square electrode (gray) positioned above a photodiode layer (dark blue) separated from the ground fractal electrode by an insulating region (light blue)

Fig. 43.3 could be used for neuron stimulation applications. Translation of these designs into brain or retinal stimulating implants would need to feature active electrodes that accommodate the high resolutions required for these applications

(the active electrodes of retinal and brain implants are typically of the order of ~20 µm and ~10 µm, respectively) [11, 57].

Here, we consider several potential approaches to achieving this. The simplest translation would be to employ the fractal electrode as the active electrode bounded by a rectangular ground electrode featuring a gap to allow passage of the active electrode to a voltage source (Fig. 43.7a). In this application, the voltage source would bias the active electrode and the electric field generated between the active and the ground electrode would be used to stimulate the neurons. However, the active electrode would need to be scaled down or subdivided into component electrodes to match the sizes of the typical brain implants. A more appealing approach, applicable to retinal implants, would use the large-scale fractal as the ground electrode with an array of small holes defined along its branches (Fig. 43.7b). Each hole would then encapsulate an active square electrode deposited above a photodiode layer that is separated from the ground electrode by an insulator [54, 58]. In this application, light-induced charge in the photodiode migrates up to the active electrode and generates the electric field between this and the ground electrode. The square active electrodes could be replaced by fractal electrodes to further increase their electrical capacitance and hence their ability to stimulate the neurons [54, 55].

In terms of electronic sensors, the simultaneous occurrence of many neuronal signals makes tracking individual signals extremely difficult. This problem is analogous to the "cocktail party problem" when the listener tries to focus on a specific conversation among the background "chatter" from many guests. To accomplish this task, recordings from the conventional sensors are analyzed using waveform analysis or triangulation to determine signal location. Waveform analysis relies on a priori information about signals' temporal characteristics (their waveforms) to identify unique signatures of individual neurons. In vivo, this is limited by: (1) isolating thousands of signals, (2) waveform variability within each neuron, and (3) electrode drift with time [59]. Triangulation works by measuring the waveform variation between different sensors in the array. However, errors in uniquely identifying thousands of signals present critical problems for triangulation algorithms [60]. Our fractal sensor avoids all of the aforementioned limitations by uniquely identifying neuronal signals without post-measurement analysis and its reliance on a priori information about waveforms. This is achieved by incorporating a fractal conduction network [49].

A common approach to conventional electronic sensors features a semiconductor channel that conducts electricity between source and drain terminals. The electric potential generated by neuron signals depletes electrons in the channel, leading to a measurable resistance change. Unfortunately, this traditional design offers little flexibility for improvement. For example, gains in measurement resolution by reducing device size are inevitably coupled with larger measurement noise due to increased resistance. Our bio-inspired design is shown in Fig. 43.8. Current is passed between pairs of measurement terminals through a fractal distribution of conducting channels (this active region is symbolized by the light gray square). Depletion of a local region of this network will induce a re-arrangement of current through the network. The nonlinear signature of this re-arrangement is expected to generate an
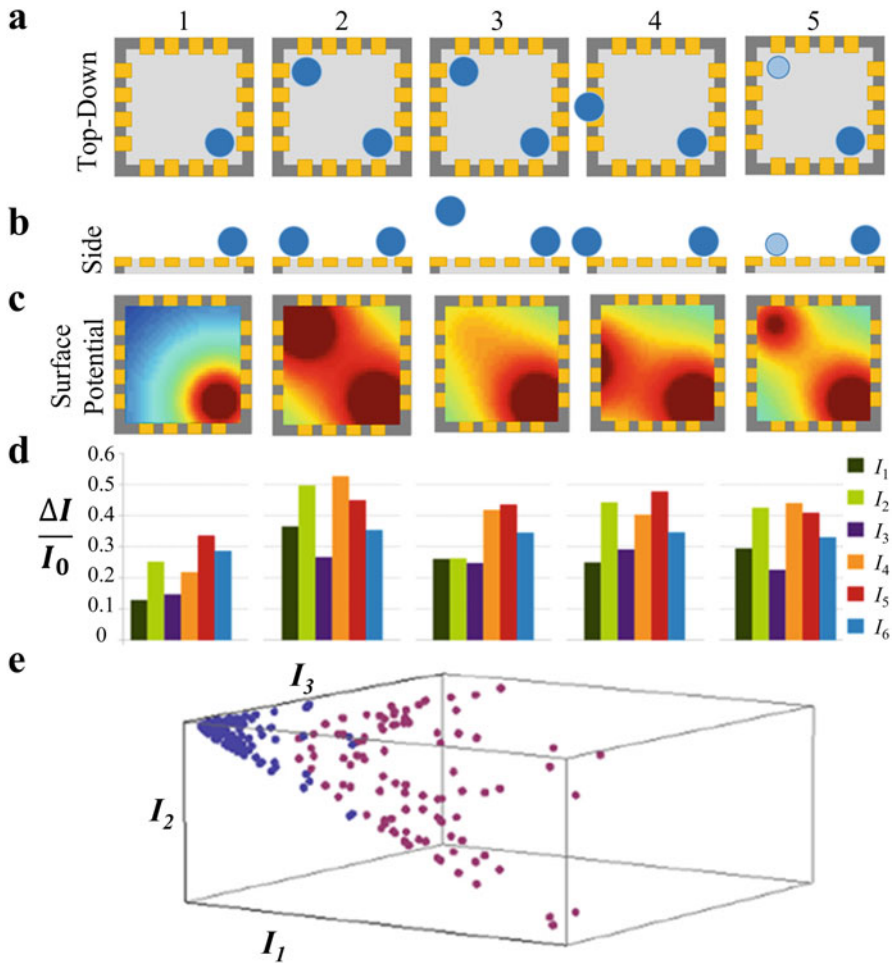
Fig. 43.8 Illustrative examples of neurons (blue) acting as electrostatic gates on the active layer (light gray) on an insulating substrate (dark gray) of a multi-electrode field effect transistor (FET) probe using 16 electrodes (gold) to serve as source and drain. Five different neuronal positions and magnitudes, shown per column, lead to unique sets of current measurements. The top-down (**a**) and side projections (**b**) of 10 μm (dark blue) or 7 μm (light blue) neurons. (**c**) The unique surface potentials associated with the (x, y, z) coordinates of neurons in each case. (**d**) The associated normalized current changes, $\Delta I/I_0 = (I - I_0)/I_0$, through specific electrodes in each case. I_0 is the electrode's current with no stimulus. (**e**) The current signatures (for three currents) are shown for one neuron at different locations and signal strengths (purple = small signal, magenta = large signal). (Figure taken from Ref. [47])

exponential sensitivity of the measured resistance to the location of the depletion region and hence to the neuronal signal. Combining the measurements from the various terminal pairs creates an emergent knowledge greater than the sum of the individual measurements. This is achieved through a calibration library that, in real

time, converts the multiple resistance values into unique values for the position and size of each signal's depletion pattern. Returning to the cocktail party analogy, the resulting enhanced sensitivity is equivalent to giving the party guests hearing aids. The calibration library is equivalent to the guests working as a team, comparing notes about previous parties.

Considering the fundamental operational principles in more detail, the 16 terminals allow for 15 independent measurements of the current in the channel. The simulations shown in Fig. 43.8 quantify the sensitivity of these 15 measurements to the location and magnitude of the electric field generated by neurons firing (their positions are indicated by the blue circles in Fig. 43.8a and b). Serving as a control, the results shown are for a uniform semiconductor channel. Five example neuron scenarios, numbered 1–5, are shown by column in Fig. 43.8. For each scenario, the resulting potentials at the sensor surface and the current between six terminals are calculated (Fig. 43.8c and d, respectively). The six current measurements show the unique current signature for each of the neuron configurations, allowing the sensor to distinguish the signal's origin and magnitude for each neuron.

The library plot shown in Fig. 43.8e is based on just three current measurements for one neuron at different locations and signal strengths. In future applications, once a library is established a search algorithm could then be used to convert the 15 measured current values into the positions and magnitudes for each neuron present. The accuracy of the sensor will depend on the degree to which scenarios can be distinguished in the library and this is determined by how the data points fill the available space. In particular, degeneracies (i.e. two scenarios occupying the same data location) will increase if data points occupy only a small fraction of the current space. If the uniform channel is replaced by a statistical fractal network, the nonlinearity of the current re-arrangement produces enhanced sensitivity of the measured current to the location of the depletion region and hence to the neuron signal. This will increase the spread of data in the current space, increasing our ability to distinguish between the unique current signatures of different neuronal scenarios.

The CNT films used to generate the statistical fractals are ideal for the sensor network because the percentage of metallic and semiconductor CNTs in the network can be adjusted with the growth conditions. This composition along with tube density are key parameters for determining the most sensitive network, and this is the subject of ongoing simulations and measurements of fabricated fractal networks. In particular, the junctions between the semiconductor and metallic CNTs form Schottky barriers and their large associated resistances cause currents to divert through neighboring routes. These form "pinch points" in the network which can radically impact the current when depleted by a neuronal signal.

43.4   The Biophilic Interface

Building on the advantageous mechanical, optical, and electrical properties proposed so far, the interconnects also provide a crucial biocompatibility function. We have already highlighted how the CNTs' chemical composition and their surface textures encourage neuronal adhesion and growth. This close proximity of an abundance of healthy neurons to the textured surface will enhance neuron stimulation for electrodes and enhance signal detection for sensors. This is analogous to attracting the party guests that you want to talk to and listen to. In contrast, smooth surfaces are known to trigger an accumulation of glial cells [35, 61, 62], to the extent of sometimes forming a protective layer called a glial scar [44]. Whereas the presence of individual glial cells is a signature of health (because they serve as the neurons' life support system), the scar pushes the neurons away from the smooth surface of conventional implants reducing their ability to stimulate or sense the neurons.

Defining a physical fractal pattern in the implant's surface exploits this difference in the responses of the two cell types and in doing so introduces an extra functionality – the ability to selectively direct neurons and glia to different locations on the interconnect. Although this is advantageous for both sensing and stimulating implants, here we will describe the H-Tree electrode of Fig. 43.3 in detail. Our aim is for neurons to adhere in large numbers to the textured VACNT branches and for glial cells to primarily cover the smooth surface of the SiO_2 gaps between them. Because of this cell "herding," the glia will be prevented from hindering neuron–electrode interactions but will be sufficiently close to provide the trophic and metabolic support necessary for the nearby neurons to maintain health and to transmit electrical signals. The electrode branches will take on the role of the physical scaffold normally provided by the glial cells when supporting neurons, ensuring neuron-rich electrodes that maximize stimulation.

Building on a broad range of CNT compatibility studies (including in vitro [36, 63], rat in vivo [58], and human ECG tests [64]), we focus on in vitro experiments due to the controlled environment in which fluorescence microscopy can be used to examine cell behavior and cell–electrode interactions as they evolve over 17 days in vitro (DIV). In our experiments, implants are lowered into a retinal co-culture of neurons and glia and imaged as the cells interact with the electrodes [43]. To prepare the culture, the retina is first removed from the outer epithelium of neonatal mice and placed in a culture medium containing enzymes, which is then mechanically agitated to dissociate the retinal cells. Subsequent staining allows the various retinal cells to be analyzed separately. DAPI (blue) fixes to the cell nuclei (allowing a total cell count), GFAP (green) attaches to glial cells, and β-tubulin III (red) binds to neuron microtubules. Based on our long-term goal of neuron stimulation and the fact that neuronal processes have a high density of stimulation sites, we focus our quantitative analysis of the neurons on the density of their processes (i.e. total length of the dendrites and axons within a given surface area). Based on their role of promoting neuron homeostasis and survival, we focus the glial analysis on their

Fig. 43.9 False-colored
SEM image highlighting cell
bodies (blue) and process
(orange) behavior for textured
VACNT and smooth SiO_2
regions. The scale bar is
$50\,\mu m$
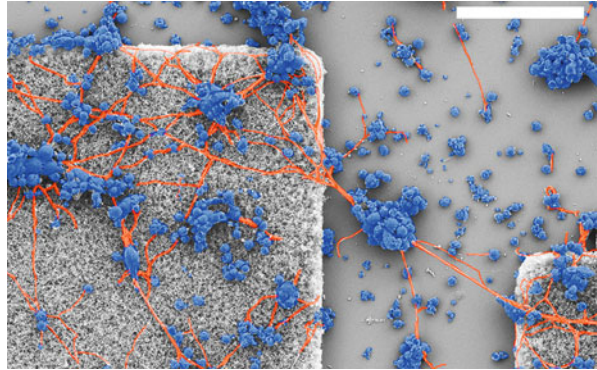
surface coverage density (referred to hereafter as "coverage," i.e. the surface area
covered by glia normalized to the total area available).

Figure 43.9 employs false coloring of an SEM image to highlight some of the
basic properties of the neurons as they interact with the textured VACNT and
smooth SiO_2 surfaces. Somas (colored blue) join to form clusters on both surfaces,
and these are connected via processes (orange) to form a network that spans both
surfaces. Figure 43.10 shows representative fluorescence microscopy images of
fractal electrodes along with Euclidean rows and grids to highlight common neuron
and glial behaviors across various electrode shapes. Whereas glial cells are observed
in the gaps, the VACNT electrodes are sufficiently high to act as barriers that are
never traversed and therefore present the potential to guide glial coverage across the
SiO_2 surface. On the rare occasions that they attach to the VACNT surfaces, they
exhibit a more branched morphology than in the gaps. On the even rarer occasions
that they coincide with 90° corners in the VACNT pattern, they are not restricted by
these turns. In terms of neuronal growth, their processes are generally considerably
longer and form more complex networks on the VACNTs. The relatively simple
networks on the SiO_2 surfaces feature fewer but larger clusters. The neuronal
processes tend to follow the top and the bottom edges of the electrodes upon
reaching them and are able to climb up or down the sidewalls to connect cell clusters
that exist on both surfaces.

Figure 43.11 provides more detailed observations of the cell responses to the
fractal electrodes. This is facilitated by categorizing the gaps into three regions
based on the cell behavior in these regions. The columns show example images
of the neurons and glia, along with schematic representations immediately below
these images: the electrode region (Fig. 43.11a, e, i-1, and j-1), the "boundary"
region (Fig. 43.11b, f, i-2, and j-2), the "cluster" region (Fig. 43.11c, g, i-3, and
j-3), and the "desert" region (Fig. 43.11d, h, i-4, and j-4). The deserts are furthest
away from the electrodes and feature a few individual neurons and small clusters
with weak processes, along with a scattering of glial cells. Nearer to the electrodes,
neurons aggregate into larger clusters physically connected to each other by bundles
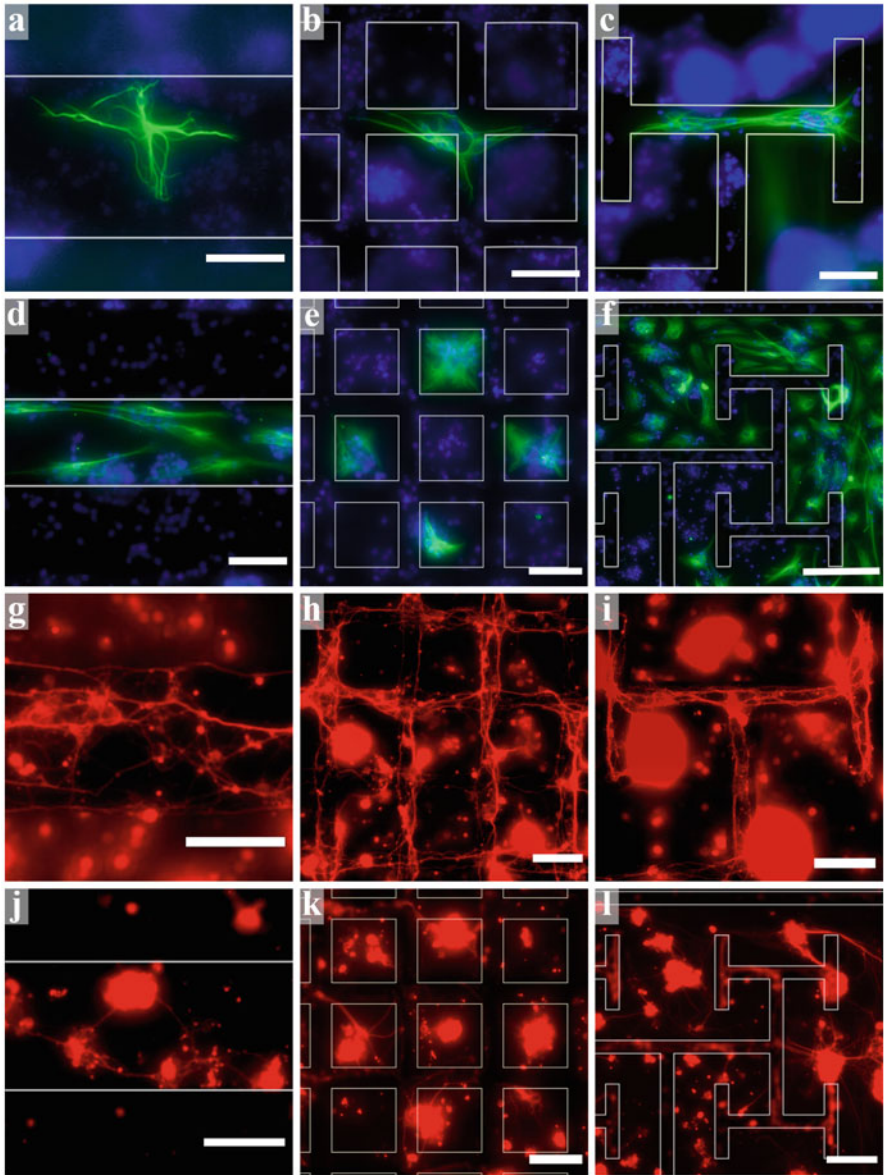of processes and accompanied by significant numbers of glia. These are labeled

Fig. 43.10 Representative examples of fluorescence images of retinal cells interacting with the row, grid, and fractal electrodes at 17 DIV (green = GFAP labeled glia; red = β-tubulin III labeled neurons; blue = DAPI labeled nuclei). Glia on the VACNT surfaces of the (**a**) row, (**b**) grid, and (**c**) fractal electrodes. Glia on the SiO_2 surfaces of the (**d**) row, (**e**) grid, and (**f**) fractal electrodes. Neuron processes following the VACNT patterns of the (**g**) row, (**h**) grid, and (**i**) fractal electrodes. Neuron clusters and processes on the SiO_2 surfaces of (**j**) row, (**k**) grid, and (**l**) fractal electrodes. Electrode edges are highlighted with white lines except for panels (**g**), (**h**), and (**i**) which concentrate on the behavior of processes along the edges because the lines would have obscured these processes. Scale bars are 50 μm in (**a**)–(**e**) and (**g**)–(**k**) and 100 μm in (**f**) and (**l**)
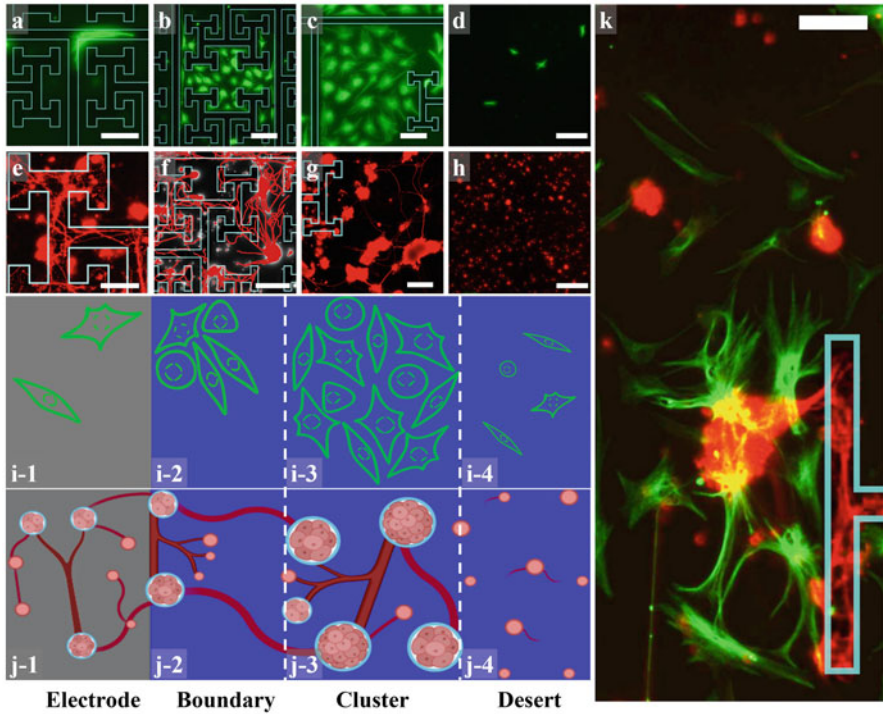
Fig. 43.11 Examples of fluorescence images of retinal cells interacting with the fractal electrodes at 17 DIV (green = GFAP labeled glia; red = β-tubulin III labeled neurons). (**a**) The rare occurrence of glia following the 90° turn of a 2–6 electrode branch. (**b**) Glial coverage in the gap of a 2–6 electrode. (**c**) Glial coverage in the gap of a 1.1–4 electrode close to its branches. (**d**) Individual glia in a desert region away from the branches of a 1.1–4 electrode. (**e**) Neurons and their processes on a 2–6 electrode's branches. (**f**) Neuron clusters and processes in a boundary region interacting with the neurons on the nearby branches of a 2–6 electrode. Neuronal processes were semi-automatically traced using the Fiji simple neurite tracer and were false-colored. (**g**) Neuron clusters and processes forming a cluster neural network in the gaps of a 1.1–4 electrode. (**h**) Individual neurons in a desert region of a 1.1–4 electrode far from the branches. (**i**) and (**j**) Schematic of the glial and neural network regions. (**i-1**) and (**j-1**) The electrode with few glial cells and multiple processes connecting individual neurons and small- to medium-sized clusters. (**i-2**) and (**j-2**) show the "boundary" region featuring small to medium glial coverage regions and clusters connecting to each other and to neurons on the electrodes using multiple processes. (**i-3**) and (**j-3**) show the "cluster" region featuring larger glial coverage and clusters with bundles of processes connecting them. (**i-4**) and (**j-4**) show the "desert" region furthest from electrodes featuring very few glial cells, mostly individual neurons and very few processes. (**k**) Merged fluorescence image of glia and neurons on a 2–4 electrode showing all the different regions. Scale bars on (**a**)–(**c**), (**f**), and (**g**) are 100 μm, on (**d**) and (**h**) are 200 μm, and on (**e**) and (**k**) are 50 μm. The electrode edges are highlighted in cyan in (**a**)–(**c**), (**e**)–(**g**), and (**k**). Schematic panels were created in BioRender. (Figure taken from Ref. [41])

as cluster regions in recognition of their typically larger clusters compared to the other regions. Many of these cluster networks are connected to neurons on the electrodes via the boundary regions, which form in some places along the electrode–gap interface. These boundary regions are composed of small- to medium-sized clusters and accompanied by occasional glial coverage. Figure 43.11k captures these various behaviors in one wide field of view and emphasizes that the cell–electrode interactions are far more subtle than the term "herding" would suggest.

The formation of these regions can be understood by recognizing the importance of surface adhesion for neuron development and their ultimate survival. In particular, neurons can aggregate into clusters reminiscent of small-world networks – so named because each node is connected to all other nodes through a small number of connecting neuronal processes, a strategy that can maximize signal transmission efficiencies [65, 66]. Initially, our neurons extend their processes in search of neighboring cells and reach a maximal complexity state featuring large numbers of nodes (individual cells and clusters) and links (neuronal processes) between them [43]. An analysis of 3, 7, and 17 DIV suggests that this peak complexity occurs around 7 DIV for our networks [43]. The network then starts to optimize as it shifts dominance from mostly neuron–substrate to neuron–neuron interaction forces also playing a large role [67]. The nodes then decrease in number as the largest clusters absorb their smaller neighbors. The links connecting them also decrease, with some processes joining together to form bundles [68] and others pruned [69]. This fine-tuning results in cluster regions displaying small-world-like networks. In contrast, neuron processes close to the electrode branches experience strong cell–VACNT adhesion forces that compete with the neuron–neuron forces, slowing down cluster formation and resulting in boundary regions. Neurons anchored to the VACNT surfaces secrete chemical signals [70]. This encourages strong interaction between neurons on the VACNTs and in the nearby gaps, leaving the gaps furthest away from electrodes to form deserts almost devoid of neurons. These developments are supported by glial cells which proliferate through cell division and growth, following chemical cues [70] that increase their surface coverage close to the neuron-rich cluster and boundary regions [71, 72]. This glial coverage supports not only neuronal survival and process development but also migration along glial fibers [73, 74] toward the electrodes.

To consider how the fractal properties of the electrodes influence the cell growth and assembly behavior (e.g. glial cell division and neuron process bundling and pruning), we introduce geometric parameters that relate these behaviors to the fractal geometry of their environment [43]. The fractal electrode design integrates two sets of related, multi-scaled patterns – the branches and the gaps – and our investigations show that both impact the cell organization favorably. The repeating patterns of the branches build long edges that interface with the gaps, and their interpenetrating nature is further amplified by their meandering character. We quantify these two branch characteristics by their total edge length E_n and Tortuosity T. We quantify the gaps by their proximities to the branches (P is the reciprocal of the distance between each gap pixel and its nearest branch pixel, averaged across all pixel locations in the gap) and various measures of gap areas. For example, A_c is the

maximum connected area of the gaps and characterizes the "openness" of the gap patterns for glial cells to cover before being blocked by intruding electrode branches [43].

Fractals with high D and m provide large E_n, T, and P but low A_c. These characteristics are predicted to encourage boundary regions and reduce desert regions, since there are no large gaps far away from branches. In contrast, fractals with low D and m generate low E_n, T, and P values but high A_c. These fractals are expected to minimize boundary regions, and their vast empty gaps will encourage deserts. Forming between the boundary and desert regions, we expect the growth of cluster regions to be encouraged for mid-D and m electrodes. Taken together, these effects suggest that fractals with mid to high D with four to five repeating levels will promote the most favorable cell interactions. They will enhance glial coverage inside the multi-scaled gaps without restricting the glia and will also prevent the creation of deserts. These glia will contribute to fuel the formation of the neural networks in the cluster regions. The large VACNT edge length of these fractals in close proximity to the SiO_2 gaps enhances the growth of neuronal processes in the boundary region connecting the cluster neural networks to those on the VACNT branches. These predictions are confirmed by qualitative inspection of the fluorescence images coupled with a detailed experimental analysis of the dependence of the cell measurements (G_{Si}, G_{CNT}, N_{Si}, and N_{CNT} – defined as glial covering area or neuron process length on each surface divided by the total area of that surface) on the fractal parameters [43].

Within this model, the advantage of H-Tree fractals over Euclidean rows and grids lies in the fact that they provide a connected electrode with an abundance of edges for neurons to follow while also allowing glial cells to cover the nearby interconnected, multi-scaled gaps. For example, Fig. 43.12 presents the balance of electrode proximity with gap openness by plotting P vs A_c for the fractal and Euclidean patterns. The high P and low A_c values of the Euclidean electrodes studied in our experiments (represented by the filled red and green symbols) are predicted to be dominated by boundary behavior. However, if Euclidean electrodes with larger gaps had been fabricated to match the fractal A_c values, their low P values are predicted to be dominated by deserts. In contrast, the fractals achieve relatively high P and A_c values simultaneously. In terms of the optimal balance of P and A_c, we note that the cluster-dominated fractals (i.e. mid to high D with four to five repeating levels) lie in the middle region of blue data.

To examine how these cell responses translate to the electrodes' ability to "herd" (i.e. for neuron processes to adhere predominantly to the electrodes and in contrast for the glia to accumulate in the gaps), we introduce key quantitative measures to build on these qualitative observations. We define N as the ratio of the total neuron process length on the electrode (N_{CNT}) to that on the combination of the electrode and gap surfaces (i.e. $N_{CNT} + N_{Si}$), where N_{CNT} and N_{Si} have been normalized relative to the surface areas of the electrode and SiO_2, respectively [43]. Similarly, we introduce G as the ratio of the glial coverage area in the gaps (G_{Si}) to that on the electrode and gap surfaces combined (i.e. $G_{CNT} + G_{Si}$), where G_{CNT} and G_{Si} have also been normalized to the surface areas of the electrode and SiO_2,
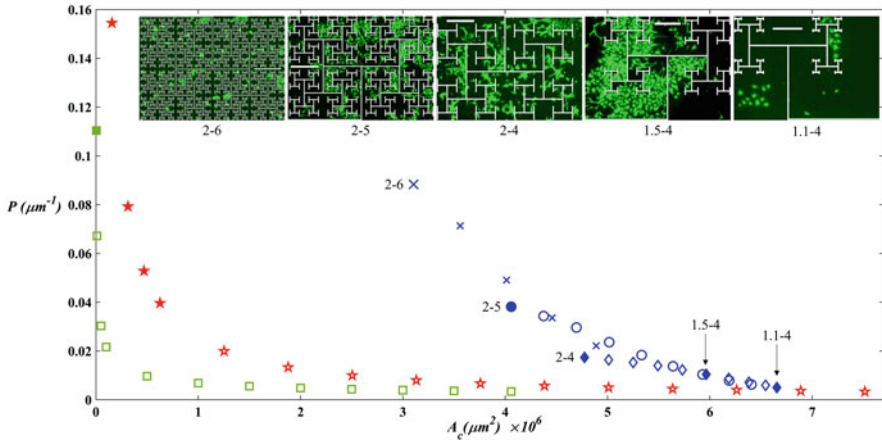
Fig. 43.12 Simulation plots of mean proximity, P, against the connected area, A_c, for fractal (blue), grid (green), and row (red) electrodes. D and m are varied for the fractals, and the W_{Si} values are varied for the rows and the grids. In each case, the filled symbols represent electrodes studied experimentally. The insets show fluorescence microscopy images of glia in the SiO_2 gaps of the fractal electrodes. Scale bars are 500 μm

respectively [43]. Adopting these measures, N and G values greater than 0.5 indicate successful guiding of neuronal processes and glial cells to the desired VACNT and SiO_2 surfaces, respectively. We also introduce the multiplication parameter GN to quantify the combined herding power.

Figure 43.13a shows a scatterplot of N vs G along with the equivalent binned data in Fig. 43.13b. Here, we group the electrodes into their three geometric categories – fractals, grids, and rows – and note that a more detailed analysis of the dependence of these categories on their parameters (e.g. D, m, W_{Si}, etc.) is presented elsewhere [43, 75]. In Fig. 43.13c–e, we also plot histograms of the percentage of electrodes within each electrode category that have given G, N, and GN values. In terms of overall herding, the fractal electrodes deliver the best GN performance (see Ref. 41 for discussions of statistical analysis). This is as expected. For example, cluster-dominated fractals generate both low N_{Si} and large G_{Si} values. In contrast, the grids have the lowest G_{Si} values because their disconnected gaps prevent the expansion of glial coverage.

Intriguingly, inspection of N reveals that the grids perform the best in terms of neuron herding. This can be understood by returning to Fig. 43.13a and b, where the dashed vertical line represents a threshold G_T in glial herding at $G \sim 0.95$, beyond which no Euclidean electrodes are observed. The superior neuron herding of the grids over the fractals is in part due to a collapse of the fractal N_{CNT} value in the high ($G > G_T$) regime. This is likely due to changes in G. Notably, in addition to some fractals supporting G_{Si} values larger than those reached in the low regime, G_{CNT} also drops when moving to the high regime. This results in G_{CNT} values significantly lower than those of the grids. It is possible that a small presence of glia
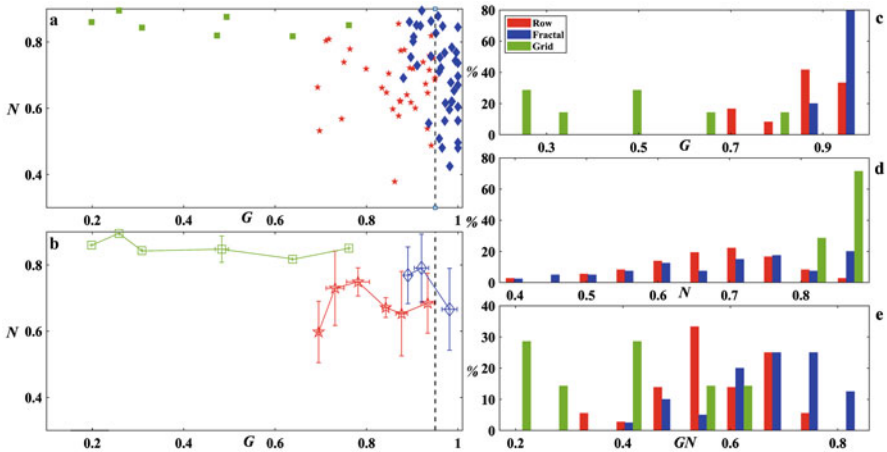
Fig. 43.13 (**a**) Scatterplot of *N* (neuron herding) vs *G* (glial herding) at 17 DIV for the row (red), fractal (blue), and grid (green) electrodes where each data point represents one electrode. (**b**) Binned average of the *N* vs *G* plot at 17 DIV for the row, fractal, and grid electrodes. In both cases, we note data that are statistical outliers have been excluded from the plots. Histograms of the percentage of electrodes with a given (**c**) *G*, (**d**) *N*, and (**e**) *GN* values at 17 DIV for the row, fractal, and grid electrodes

Fig. 43.14 N_{CNT} vs G_{Si} for the 2-5 fractals
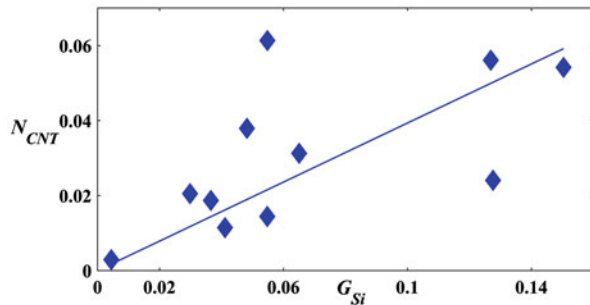
is required on the VACNT surface to support neurons and the high regime fractals fall below this minimum level. The low G_{CNT} might result from the sparse cross sections of some of the fractals, and this could be addressed by fabricating future H-Trees featuring wider branches.

A central question to herding concerns the amount of glial coverage needed in the gaps to keep neurons healthy and functional on the VACNT electrodes. In order to study the correlation between the glia inside the SiO_2 gaps and neurons on the VACNT electrodes, we plot N_{CNT} vs G_{Si} in Fig. 43.14 for the 2-5 fractal electrodes. By comparing variations within the fractal electrode, neuron process growth can be taken as an indicator of health because all other geometric factors are constant. N_{CNT} increases with G_{Si} with the shown linear fit described by an R^2 of 0.63. We use this fit to highlight the following key observations. Firstly, the data trend suggests that an
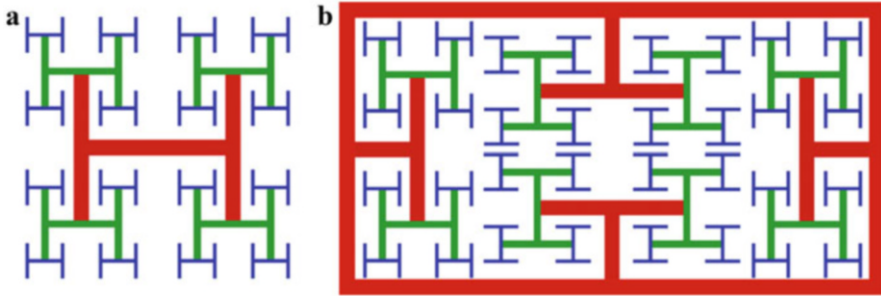
Fig. 43.15 (**a**) H-Tree fractal electrode with three magnification levels. (**b**) Optimal electrode design based on the cut and rotated parts of the electrode shown in (**a**). The whole design is bounded with the red rectangle to ensure electrode connectivity

absence of glia (i.e. $G_{Si} = 0$) impedes the growth of neuron processes substantially. However, the data does not reveal a distinct lower limit (i.e. a G_{Si} value below which N_{CNT} falls to zero). This is backed up by qualitative observations showing that there are some VACNT regions that support processes even in the absence of nearby glia. Secondly, when variations in G_{Si} within the culture result in more glia, this increased presence promotes neuronal growth. Our 17 DIV fractal system operates within a regime in which there is no upper limit – the more glia the better.

The absence of an upper limit suggests that refined electrode designs that increase G_{Si} will further boost neuron health and perhaps even remove the need for the small presence of glia on the VACNT surface. As an example of refinement, rather than branches spreading out from the origin as done in the H-Tree used in our study (Fig. 43.15a), the branches shown in Fig. 43.15b spread from a boundary inward. Removing branches from the central section of the design creates a completely connected SiO_2 gap region while keeping the proximity of the gaps to the electrodes roughly comparable to the original fractal electrode. We predict that optimized designs will ensure that a larger number of neuronal processes reside within the stimulating fields generated when the electrode branches are electrically biased. The stimulated processes will connect to neurons in the gaps that resemble small-world networks, improving the electrode's ability to stimulate the surrounding retinal neurons more efficiently. Furthermore, in contrast to implants that use anti-inflammatory drugs to inhibit glial scarring on their electrode [76], glial cells will be confined to the gaps between our electrodes where their proximity to the neurons will ensure the neurons' health, prolonging the stability and functionality of the retina–implant interface.

43.5   Conclusions

In this chapter, we have discussed some of the key favorable properties of fractal interconnects designed to interact with neural networks. The term "interconnect" emphasizes the multi-functional character of this interface. Accordingly, we have considered their mechanical, optical, and electrical properties along with their ability to promote positive cell interactions. These properties are applicable to interconnects used to stimulate and sense signals in the neural network. Future experiments will be aimed at confirming the enhanced performance of fractal designs over conventional Euclidean designs – in particular, quantifying their electrical and biophilic advantages. Our approach of integrating computer modeling with in vitro studies allowed controlled investigations to establish the fundamental performances of these inherently complex systems. However, a vital step forward will be to focus on transferring these studies to the in vivo environment.

Fractal implants have much to offer. Brain implants could be used to address a number of pathological conditions including Parkinson's disease. In addition, they could also radically improve other stimulation techniques to improve learning and cognition, visual perception, working memory, and motor control [77]. Retinal implants could be used to regain vision lost due to diseases such as macular degeneration or retinitis pigmentosa. The long-term potential impact of fractal interconnects could also stretch well beyond improving implants designed to interact with the human brain, retina, and limbs. In addition to stimulating and sensing naturally occurring neurons, they could be applied to retinal STEM cells in both in vitro and in vivo investigations.

Complementing the above medical applications, the central question asked in this chapter – what do we gain by building interconnects that match the fractal properties of the cells they interact with – also addresses the basic science of cell behavior and electricity. Fueled by technology, the prospect of fractal implants demonstrates how far electronics has come from the days of Franklin harnessing electricity from the clouds, and Le Roy and Galvani applying it to the human body.

References

1. Lewis PM, Rosenfeld JV. Electrical stimulation of the brain and the development of cortical visual prostheses: an historical perspective. Brain Res. 2016;1630:208–24.
2. Marlow CA, et al. Unified model of fractal conductance fluctuations for diffusive and ballistic semiconductor devices. Phys Rev B. 2006;73:195318.
3. Micolich AP, et al. Evolution of fractal patterns during a classical-quantum transition. Phys Rev Lett. 2001;87:036802.
4. Sachrajda AS, et al. Spin-controlled resonances in the magnetotransport in quantum dots. Phys Rev B. 1993;47:6811–4.
5. Taylor RP, Sachrajda AS, Zawadzki P, Coleridge PT, Adams JA. Aharonov-Bohm oscillations in the Coulomb blockade regime. Phys Rev Lett. 1992;69:1989–92.
6. Jang J, et al. Implantation of electronic visual prosthesis for blindness restoration. Opt Mater Express. 2019;9:3878–94.
7. Chenais NAL, Airaghi Leccardi MJI, Ghezzi D. Photovoltaic retinal prosthesis restores high-resolution responses to single-pixel stimulation in blind retinas. Commun Mater. 2021;2:1–16.
8. Prévot P-H, et al. Behavioural responses to a photovoltaic subretinal prosthesis implanted in non-human primates. Nat Biomed Eng. 2020;4:172–80.
9. Tong W, Meffin H, Garrett DJ, Ibbotson MR. Stimulation strategies for improving the resolution of retinal prostheses. Front Neurosci. 2020;14:262.
10. Lorach H, et al. Photovoltaic restoration of sight with high visual acuity. Nat Med. 2015;21:476–82.
11. Palanker D, Le Mer Y, Mohand-Said S, Muqit M, Sahel JA. Photovoltaic restoration of central vision in atrophic age-related macular degeneration. Ophthalmology. 2020;127:1097–104.
12. Palanker D, Le Mer Y, Mohand-Said S, Sahel JA. Simultaneous perception of prosthetic and natural vision in AMD patients. Nat Commun. 2022;13:513.
13. Edwards TL, et al. Assessment of the electronic retinal implant alpha AMS in restoring vision to blind patients with end-stage retinitis pigmentosa. Ophthalmology. 2018;125:432–43.
14. Hariz M. My 25 stimulating years with DBS in Parkinson's disease. J Parkinsons Dis. 2017;7:S33–41.
15. Fan X, Agid Y. At the origin of the history of glia. Neuroscience. 2018;385:255–71.
16. Von Bartheld CS, Bahney J, Herculano-Houzel S. The search for true numbers of neurons and glial cells in the human brain: a review of 150 years of cell counting. J Comp Neurol. 2016;524:3865–95.
17. Zhang Y, Barres BA. Astrocyte heterogeneity: an underappreciated topic in neurobiology. Curr Opin Neurobiol. 2010;20:588–94.
18. Smith JH, et al. How neurons exploit fractal geometry to optimize their network connectivity. Sci Rep. 2021;11:2332.
19. Rowland C, et al. Investigating fractal analysis as a diagnostic tool that probes the connectivity of hippocampal neurons. Front Physiol. 2022;13:932598.
20. Rowland C, et al. Neuron arbor geometry is sensitive to the fractal properties of their dendrites. Front Netw Physiol. 2023;3:1072815.
21. Seidel D, et al. How a measure of tree structural complexity relates to architectural benefit-to-cost ratio, light availability, and growth of trees. Ecol Evol. 2019;9:7134–42.
22. Hou C, Gheorghiu S, Huxley VH, Pfeifer P. Reverse engineering of oxygen transport in the lung: adaptation to changing demands and resources through space-filling networks. PLoS Comput Biol. 2010;6:e1000902.
23. Bronikowski MJ. CVD growth of carbon nanotube bundle arrays. Carbon. 2006;44:2822–32.
24. Yunyu W, Li B, Ho P, Yao Z, Shi L. Effect of supporting layer on growth of carbon nanotubes by thermal chemical vapor deposition. Appl Phys Lett. 2006;89:183113.
25. Zhao B, et al. Exploring advantages of diverse carbon nanotube forests with tailored structures synthesized by supergrowth from engineered catalysts. ACS Nano. 2009;3:108–14.
26. Chen Y-C, et al. An active, flexible carbon nanotube microelectrode array for recording electrocorticograms. J Neural Eng. 2011;8:034001.

27. David-Pur M, Bareket-Keren L, Beit-Yaakov G, Raz-Prag D, Hanein Y. All-carbon-nanotube flexible multi-electrode array for neuronal recording and stimulation. Biomed Microdevices. 2014;16:43–53.
28. Bareket-Keren L, Hanein Y. Carbon nanotube-based multi electrode arrays for neuronal interfacing: progress and prospects. Front Neural Circuits. 2013;6:22.
29. Fabbro A, Bosi S, Ballerini L, Prato M. Carbon nanotubes: artificial nanomaterials to engineer single neurons and neuronal networks. ACS Chem Neurosci. 2012;3:611–8.
30. Krukiewicz K, Janas D, Vallejo-Giraldo C, Biggs MJP. Self-supporting carbon nanotube films as flexible neural interfaces. Electrochim Acta. 2019;295:253–61.
31. Hu H, Ni Y, Montana V, Haddon RC, Parpura V. Chemically functionalized carbon nanotubes as substrates for neuronal growth. Nano Lett. 2004;4:507–11.
32. Nick C, Yadav S, Joshi R, Thielemann C, Schneider JJ. Growth and structural discrimination of cortical neurons on randomly oriented and vertically aligned dense carbon nanotube networks. Beilstein J Nanotechnol. 2014;5:1575–9.
33. Sorkin R, et al. Process entanglement as a neuronal anchorage mechanism to rough surfaces. Nanotechnology. 2009;20:015101.
34. Flanagan LA, Ju Y-E, Marg B, Osterfield M, Janmey PA. Neurite branching on deformable substrates. Neuroreport. 2002;13:2411–5.
35. Georges PC, Miller WJ, Meaney DF, Sawyer ES, Janmey PA. Matrices with compliance comparable to that of brain tissue select neuronal over glial growth in mixed cortical cultures. Biophys J. 2006;90:3012–8.
36. Watterson WJ, et al. The roles of an aluminum underlayer in the biocompatibility and mechanical integrity of vertically aligned carbon nanotubes for interfacing with retinal neurons. Micromachines (Basel). 2020;11:546.
37. Gabay T, et al. Carbon nanotube based neuro-chip for engineering, recording and stimulation of cultured networks. In: The 13th international conference on solid-state sensors, actuators and microsystems, 2005. Digest of technical papers. TRANSDUCERS '05, vol. 2. IEEE; 2005. p. 1226–9.
38. Wang K, Fishman HA, Dai H, Harris JS. Neural stimulation with a carbon nanotube microelectrode array. Nano Lett. 2006;6:2043–8.
39. Mazzatenta A, et al. Interfacing neurons with carbon nanotubes: electrical signal transfer and synaptic stimulation in cultured brain circuits. J Neurosci. 2007;27:6931–6.
40. Cellot G, et al. Carbon nanotubes might improve neuronal performance by favouring electrical shortcuts. Nat Nanotechnol. 2009;4:126–33.
41. Lovat V, et al. Carbon nanotube substrates boost neuronal electrical signaling. Nano Lett. 2005;5:1107–10.
42. Fairbanks MS, Taylor RP. Measuring the scaling properties of temporal and spatial patterns: from the human eye to the foraging albatross. In: Nonlinear dynamical systems analysis for the behavioral sciences using real data. Boca Raton: CRC Press; 2010.
43. Moslehi S, et al. Controlled assembly of retinal cells on fractal and Euclidean electrodes. PLoS One. 2022;17:e0265685.
44. Butterwick A, et al. Effect of shape and coating of a subretinal prosthesis on its integration with the retina. Exp Eye Res. 2009;88:22–9.
45. Thanihaichelvan M, et al. Metallic-semiconducting junctions create sensing hot-spots in carbon nanotube FET aptasensors near percolation. Biosens Bioelectron. 2019;130:408–13.
46. Plank NOV, Ishida M, Cheung R. Positioning of carbon nanotubes using soft-lithography for electronics applications. J Vac Sci Technol B. 2005;23:3178–81.
47. Zheng HY, Plank NOV. Facile fabrication of carbon nanotube network thin film transistors for device platforms. Int J Nanotechnol. 2017;14:505–18.
48. Thanihaichelvan M, et al. Data on liquid gated CNT network FETs on flexible substrates. Data Brief. 2018;21:276–83.
49. Browning LA, et al. Investigation of fractal carbon nanotube networks for biophilic neural sensing applications. Nanomaterials. 2021;11:636.
50. Fan JA, et al. Fractal design concepts for stretchable electronics. Nat Commun. 2014;5:3266.

51. Zhang J, et al. Integrated device for optical stimulation and spatiotemporal electrical recording of neural activity in light-sensitized brain tissue. J Neural Eng. 2009;6:055007.
52. Zrenner E. Will retinal implants restore vision? Science. 2002;295:1022–5.
53. Cogan SF. Neural stimulation and recording electrodes. Annu Rev Biomed Eng. 2008;10:275–309.
54. Watterson WJ, Montgomery RD, Taylor RP. Fractal electrodes as a generic interface for stimulating neurons. Sci Rep. 2017;7:6717.
55. Watterson WJ, Montgomery RD, Taylor RP. Modeling the improved visual acuity using photodiode based retinal implants featuring fractal electrodes. Front Neurosci. 2018;12:277.
56. Charlier J-C, Blase X, Roche S. Electronic and transport properties of nanotubes. Rev Mod Phys. 2007;79:677–732.
57. Obaid A, et al. Massively parallel microwire arrays integrated with CMOS chips for neural recording. Sci Adv. 2020;6:eaay2789.
58. Pampaloni NP, et al. Sculpting neurotransmission during synaptic development by 2D nanostructured interfaces. Nanomedicine. 2018;14:2521–32.
59. Einevoll GT, Franke F, Hagen E, Pouzat C, Harris KD. Towards reliable spike-train recordings from thousands of neurons with multielectrodes. Curr Opin Neurobiol. 2012;22:11–7.
60. Buzsáki G. Large-scale recording of neuronal ensembles. Nat Neurosci. 2004;7:446–51.
61. Piret G, Perez M-T, Prinz CN. Support of neuronal growth over glial growth and guidance of optic nerve axons by vertical nanowire arrays. ACS Appl Mater Interfaces. 2015;7:18944–8.
62. Chapman CAR, Chen H, Stamou M, Lein PJ, Seker E. Mechanisms of reduced astrocyte surface coverage in cortical neuron-glia co-cultures on nanoporous gold surfaces. Cell Mol Bioeng. 2016;9:433–42.
63. Mata D, et al. Diels–Alder functionalized carbon nanotubes for bone tissue engineering: in vitro/in vivo biocompatibility and biodegradability. Nanoscale. 2015;7:9238–51.
64. Abu-Saude M, Morshed BI. Characterization of a novel polypyrrole (PPy) conductive polymer coated patterned vertical CNT (pvCNT) dry ECG electrode. Chemosensors. 2018;6:27.
65. Latora V, Marchiori M. Economic small-world behavior in weighted networks. Eur Phys J B. 2003;32:249–63.
66. Achard S, Bullmore E. Efficiency and cost of economical brain functional networks. PLoS Comput Biol. 2007;3:e17.
67. Liu J, et al. Control of neuronal network organization by chemical surface functionalization of multi-walled carbon nanotube arrays. Nanotechnology. 2011;22:195101.
68. Shefi O, Golding I, Segev R, Ben-Jacob E, Ayali A. Morphological characterization of in vitro neuronal networks. Phys Rev E. 2002;66:021905.
69. Luo L, O'Leary DDM. Axon retraction and degeneration in development and disease. Annu Rev Neurosci. 2005;28:127–56.
70. Fields RD, Stevens-Graham B. New insights into neuron-glia communication. Science. 2002;298:556–62.
71. Shein M, et al. Engineered neuronal circuits shaped and interfaced with carbon nanotube microelectrode arrays. Biomed Microdevices. 2009;11:495–501.
72. Villegas JC, et al. Multiwalled carbon nanotubes hinder microglia function interfering with cell migration and phagocytosis. Adv Healthc Mater. 2014;3:424–32.
73. Hatten ME, Mason CA. Mechanisms of glial-guided neuronal migration in vitro and in vivo. Experientia. 1990;46:907–16.
74. Fishell G, Hatten ME. Astrotactin provides a receptor system for CNS neuronal migration. Development. 1991;113:755–65.
75. Moslehi S, et al. Comparison of fractal and grid electrodes for studying the effects of spatial confinement on dissociated retinal neuronal and glial behavior. Sci Rep. 2022;12:17513.
76. Zhong Y, Bellamkonda RV. Dexamethasone-coated neural probes elicit attenuated inflammatory response and neuronal loss compared to uncoated neural probes. Brain Res. 2007;1148:15–27.
77. Fox D. Neuroscience: brain buzz. Nature. 2011;472:156–9.